Journal of Geophysical Research: Planets

RESEARCH ARTICLE
10.1029/2017JE005497

Key Points:
- In spherical shells the appearance of stagnant-lid convection is dependent on relative core size
- Mean temperature decreases in stagnant-lid convection systems as relative core size is decreased
- Mean temperatures in 2-D and 3-D stagnant-lid systems diverge as relative core size is decreased

Supporting Information:
- Supporting Information S1
- Figure S1

Correspondence to:
J. P. Lowman,
lowman@utsc.utoronto.ca

Citation:
Guerrero, J. M., Lowman, J. P., Deschamps, F., & Tackley, P. J. (2018). The influence of curvature on convection in a temperature-dependent viscosity fluid: Implications for the 2-D and 3-D modeling of moons. *Journal of Geophysical Research: Planets*, *123*, 1863–1880. https://doi.org/10.1029/2017JE005497

Received 24 NOV 2017
Accepted 2 MAY 2018
Accepted article online 15 MAY 2018
Published online 26 JUL 2018

The Influence of Curvature on Convection in a Temperature-Dependent Viscosity Fluid: Implications for the 2-D and 3-D Modeling of Moons

J. M. Guerrero[1], J. P. Lowman[2], F. Deschamps[3], and P. J. Tackley[4]

[1]Department of Physics, University of Toronto, Toronto, Ontario, Canada, [2]Department of Physical and Environmental Sciences, University of Toronto, Scarborough, Toronto, Ontario, Canada, [3]Institute of Earth Sciences, Academia Sinica, Taipei, Taiwan, [4]Department of Earth Sciences, ETH-Zurich, Zurich, Switzerland

Abstract Convection in terrestrial bodies occurs within spherical shells described by the ratio, f, of their bounding radii. Previous studies that have modeled convection with a temperature-dependent viscosity noted the strong effect of f on transition to the stagnant-lid regime. Here we analyze stagnant-lid convection in 2-D and 3-D systems with curvatures including relatively small-core shells (f as small as 0.2) as well as in thin shell and plane-layer cases. Several peculiarities of convection in a strongly temperature-dependent viscosity fluid are identified for both high and low curvature systems. We demonstrate that effective Rayleigh numbers may differ by orders of magnitude in systems with different curvatures, when all other parameters are maintained at fixed values. Furthermore, as f is decreased, the nature of stagnant-lid convection in small-core bodies shows a divergence in the temperature and velocity fields found for 2-D annulus and 3-D spherical shell systems. In addition, substantial differences in the behavior of thin shell ($f = 0.9$) and plane-layer (Cartesian geometry) models occur in both 2-D and 3-D, indicating that the latter (emulating a toroidal topology rather than spherical) may be inappropriate approximations for modeling variable viscosity convection in thin spherical shells. Our findings are especially relevant to understanding and accurately modeling the thermal structure that may exist in bodies characterized by thin shells (e.g., $f = 0.9$) or relatively small cores, such as shells comprising the Galilean satellites and other moons.

1. Introduction

Convection in the cryoshells of icy satellites and silicate mantles of rocky moons and planets is characterized by a strongly temperature-dependent viscosity that can result in the formation of an immobile (or stagnant) conductive lid at the top of the upper thermal boundary layer of the system. Formation of a stagnant lid occurs for heating conditions ranging from entirely internal to purely basal and is dependent on both total energy input (i.e., internal heating rate and the rate of basal heat input) and the gradient of the viscosity variation with temperature. The formation of the stagnant lid (Christensen, 1984; Reese et al., 1999; Solomatov, 1985; Solomatov & Moresi, 1996) also requires that a critical viscosity contrast must be established between the cold fluid at the surface of the shell and the warm fluid in the system's interior. Consequently, the onset of stagnant-lid convection (SLC) is a function of multiple parameters affecting the mean temperature of the convecting fluid.

Multiple studies have worked toward quantifying the dependence of mean temperature and heat flux on mantle geometry and energy input in both vigorously convecting isoviscous (Choblet, 2012; Deschamps et al., 2010; Jarvis, 1993; Jarvis et al., 1995; Moore, 2008; Shahnas et al., 2008; Sotin & Labrosse, 1999; Vangelov & Jarvis, 1994; Weller et al., 2016) and temperature-dependent viscosity systems (Deschamps & Lin, 2014; Yanagisawa et al., 2016; Yao et al., 2014). Findings show that system geometry, like rheological character, affect temperature and heat loss as strongly as the energy input associated with the heat sources. In addition, system properties may affect mean temperature differently depending on the geometry. For example, an increase in lower mantle viscosity (due to the effect of pressure) has a geometry-dependent impact on mean temperature and convective regime (O'Farrell et al., 2013).

Exact conditions required for SLC (and conversely a mobile surface) therefore remain somewhat equivocal. Furthermore, the parameterization of mean temperature and heat flow differs in two-dimensional systems versus three dimensions. Cartesian geometry studies have found that the behavior inferred from the analysis of 2-D convection models may diverge from the parameterizations obtained from 3-D convection studies (Deschamps & Lin, 2014). Hernlund and Tackley (2008) found that output diagnostics (i.e., mean temperature and Nusselt number) for 2-D spherical annulus calculations are within 5% of the values obtained in identical calculations performed in a 3-D spherical shell geometry. However, their study only focused on investigation of an Earth-like core-to-planet radius ratio.

Geometrical analogues of spherical shell convection such as convection in cylinders and axisymmetric spheres were first used to study the influence of curvature and aspect ratio on mean temperature and Nusselt number (Jarvis, 1993; Vangelov & Jarvis, 1994). The controlling parameter that determines the degree of curvature is the ratio of core radius (R_{core}) to outer shell radius (R_{outer}), $f(= R_{core}/R_{outer})$. The difference in radii is the layer depth, $d(= R_{outer} - R_{core})$. Jarvis et al. (1995) explored the influence of relative core size on temperature and convective planform in isoviscous systems and found convection in cold spherical shells characterized by a single plume rising from the core when f is 0.3 or less. Yao et al. (2014) reported similar planforms with viscosity contrasts up to 10^5 but relatively low effective Rayleigh numbers. These authors derived parameterizations for the interior temperature and heat flux in variable core size spherical shell SLC (Yao et al., 2014) heated solely by an isothermal core. However, they note the absence of SLC when $f \leq 0.4$ in systems featuring parameter values that result in SLC when f is larger (Yao et al., 2014).

The nature of convection, whether occurring presently or in the past, in bodies with small-core radii relative to the thickness of the overlying shell may be particularly relevant to the evolution of the icy satellites of the outer solar system and Earth's Moon. Estimates of the f ratio for Io's silicate mantle range from approximately 0.4–0.5 (Sohl et al., 2002), while the ratio of the inner to outer radii of Europan silicate mantle, between its metallic core and outer ice shell, is estimated to be between 0.3 and 0.4 (Schubert et al., 2009), although arguments for a Europan silicate mantle with f in the range 0.1 to 0.5 exist (Sohl et al., 2002). Uncertainty in the thickness of Ganymede's outer icy shell means that the f ratio of its silicate mantle is also difficult to constrain. Upper bounds on the thickness of its outer layer imply that it has an f ratio of 0.4 at the most (Sohl et al., 2002). Estimates of the f ratio in the icy shells of medium-sized icy satellites like Miranda range from 0.25 to greater than 0.5, dependent upon the partitioning of rock to ice in the body's core (Hammond & Barr, 2014). Much tighter constraints exist on the radius of the core of the Earth's Moon. Recent analysis of Apollo era lunar seismological data (Weber et al., 2011) suggests that the Moon harbors a small inner core. The inferred f ratio for the Moon's silicate mantle is approximately 0.2 (e.g., Matsuyama et al., 2016).

Cryoshells comprising the outermost layer of most icy moons are estimated to range in thickness from 10 to 200 km, resulting in a spherical shell geometry where f is greater than 0.8 (Barr, 2008; Hammond & Barr, 2014; Nimmo et al., 2003). Convective regimes hypothesized in these bodies range from possibly mobile and plate-like on Europa (Kattenhorn & Prockter, 2014), to either episodic (O'Neill & Nimmo, 2010) or simply sluggish-lid on Enceladus and Ganymede (Barr, 2008; Hammond & Barr, 2014), to SLC on the midsized icy moons of Saturn (Multhaup & Spohn, 2007). Because the shells are so thin, modelers commonly use small plane-layer calculations to investigate the nature of convection in these bodies. However, the limitation on convective wavelength in Cartesian boxes may artificially influence convective regimes. Moreover, plane-layer geometries have a toroidal topology rather than spherical.

With recognition that the role of initial conditions is sometimes important in determining convective regime (Crowley & O'Connell, 2012; O'Neill et al., 2016; Weller et al., 2015), robust conclusions regarding the impact of the relative core size on the mean temperature in a convecting shell of fluid may still be reached. In the study presented here, we focus on differences in the transition to and character of SLC that are found with different f values. We extend previous work by focusing on SLC in relatively small-core bodies and comparisons of Cartesian systems to global thin shell models. As f decreases, obtaining SLC requires the specification of higher viscosity contrast. To identify the parameters leading to SLC, we perform a large number of simulations of convection in a spherical annulus geometry (Hernlund & Tackley, 2008). Upon identifying parameters that yield SLC in cases featuring small cores we then examine a small number of 3-D models and compare their thermal properties to those found in 2-D calculations featuring identical parameters.

2. Method

Thermally driven convection in a Boussinesq fluid with infinite Prandtl number is modeled in two-dimensional spherical annulus and three-dimensional spherical shell geometries. A hybrid finite-difference/finite-volume code, StagYY (Tackley, 2008) solves the governing equations using a parallelized multigrid method. The flow is modeled implementing the nondimensional form of the conservation of mass, momentum, and energy equations:

$$\nabla \cdot \mathbf{u} = 0, \tag{1}$$

$$-\nabla P + \nabla \cdot \left(\eta(\nabla \mathbf{u} + \nabla \mathbf{u}^T)\right) = -\mathrm{Ra} T \hat{\mathbf{r}}, \tag{2}$$

and

$$\frac{\partial T}{\partial t} = \nabla^2 T - \mathbf{u} \cdot \nabla T, \tag{3}$$

respectively.

The nondimensional parameters are time, t; the velocity field, $\mathbf{u}$; the nonhydrostatic pressure, P; the dynamic viscosity, η; the temperature, T; and the Rayleigh number,

$$\mathrm{Ra} = \rho_0 g \alpha \Delta T d^3 / \eta^* \kappa, \tag{4}$$

which determines the convective vigor of the system. The parameters comprising Ra include g, the acceleration due to gravity; α, the thermal expansion coefficient; η^*, a reference viscosity; κ, the system's thermal diffusivity; and ΔT, the superadiabatic temperature difference across the shell thickness, d. Our calculations emulate convection in a planetary mantle or ice shell. Consequently, we shall refer to the system's boundaries as the surface and core-mantle boundary (CMB). The surface and CMB are modeled as free slip in each calculation and are isothermally fixed to nondimensional temperatures of $T = 0$ and $T = 1$, respectively. Consequently, secular cooling is not modeled. Dimensional temperatures are obtained from nondimensional temperatures through multiplying T by ΔT and adding the surface temperature, T_{surf}. For the remainder of this work we shall use T to represent the dimensional temperature.

A linearized (Boussinesq) equation of state, $\rho(T) = \rho_0(1 - \alpha(T - T_0))$, describes the density ρ as a function of temperature where ρ_0 is the density at dimensional temperature $T = T_0$. The controlling parameters that determine the convective regime are the ratio of core radius (R_{core}) to outer shell radius (R_{outer}), $f(= R_{\mathrm{core}}/R_{\mathrm{outer}})$, the reference Rayleigh number, Ra (equation (4)) and the rheology law describing how the viscosity depends on temperature. The dimensional reference viscosity η^* appearing in the Rayleigh number has a nondimensional value of 1.0 and corresponds to a dimensional reference temperature of T^* (unless stated otherwise $T^* = T_{\mathrm{surf}} + 0.5\Delta T$ in the calculations presented, corresponding to a nondimensional temperature of 0.5, and T_{surf} is the dimensional surface temperature held fixed throughout the study). We model an exponential increase in viscosity with decreasing temperature but employ a linearized approximation for the T^{-1} (Arrhenius) dependence of the argument of the exponential on T (usually referred to as a Frank-Kamenetskii rheology (King, 2009; Noack & Breuer, 2013; Solomatov, 1995; Stein et al., 2013)). Specifically, the viscosity is

$$\eta(T) = \eta^* \exp(-\gamma(T - T^*)/\Delta T). \tag{5}$$

Following this approach, the viscosity contrast across the system from top to bottom is $\Delta\eta_T = \exp(\gamma)$.

For each geometry (i.e., f value) examined, unless stated otherwise, we begin with an isoviscous rheology and an initial condition that is conductive with random perturbations. Upon reaching a steady state, a temperature field snapshot is used as the initial condition for the next case in the suite of calculations in which $\Delta\eta_T$ is systematically increased.

All of the results presented are from solutions that are thermally stable. Calculations are integrated forward until a statistically steady state is achieved. Global energy balance provides a convergence criterion that is obtained by comparing the difference in nondimensional surface and bottom heat flux (F_{top} and F_{bot}, respectively). Specifically, if F_{top} and F_{bot} for the system are steady then

$$F_{\mathrm{top}} = F_{\mathrm{bot}} f^2. \tag{6}$$

We determine that a calculation has reached a statistically steady state when the left and right-hand side of equation (6) agree to within a difference of less than 1% over an integration period of at least 10 transit times (where the transit time is defined as $t_t = d/V_{\mathrm{rms}}$ and V_{rms} is the volume averaged root-mean-square [rms] velocity of the system). Time averages of model output reported below are performed over at least 10 transit times satisfying the above heat flux criterion.

A middepth Rayleigh number, $\mathrm{Ra_m}$, is obtained when the time-averaged middepth temperature is used to evaluate the viscosity at middepth and this quantity replaces η^* in equation (4). Using equation (5) the middepth Rayleigh number becomes

$$\mathrm{Ra_m} = \mathrm{Ra}\exp(\gamma\theta_{\mathrm{m}}), \tag{7}$$

where $\theta_{\mathrm{m}} = (T_{\mathrm{m}} - T^*)/\Delta T$ is the nondimensional temperature difference between the average dimensional middepth temperature, T_{m}, and the reference temperature (this is effectively identical to the temperature in the well-mixed adiabatic interiors of stagnant-lid systems, often described in other studies). Temperatures for the well-mixed interiors are not known a priori so that the convective vigor quantified by $\mathrm{Ra_m}$ is only known once steady solutions are obtained.

The rms surface velocity V_{surf} and volumetric velocity V_{rms} provide metrics for determining whether a system has converged to a stagnant-lid mode of convection; specifically, the mobility $M = V_{\mathrm{surf}}/V_{\mathrm{rms}}$ (e.g., Stein et al., 2013; Tackley, 2000). Previous authors investigating Cartesian geometry systems (e.g., Stein et al., 2014; Tackley, 2000) have stated that $M > 0.9$ characterizes a mobile-lid convection regime. That is, cases where surface velocity magnitude is comparable to or greater than mean interior velocity magnitude are considered mobile. In this study, we adopt $M \geq 1.0$ as a threshold above which a system is designated mobile and note that isoviscous cases are mobile by this criterion for all f values modeled. If $M < 0.01$, we consider the system to be in the stagnant-lid regime. Intermediate values of M correspond to a transitional regime. Stein et al. (2013) consider values of $M < 0.01$ and $V_{\mathrm{surf}} < 1$ as necessary conditions for the system to be identified as stagnant lid. Throughout this study we also identify stagnant-lid cases where the condition on V_{surf} is satisfied as well as the criterion for M.

We extend previous studies by exploring spherical geometries with different f for basally heated convection. Unless stated otherwise, each calculation investigated has a fixed $\mathrm{Ra} = 3.2 \times 10^5$. Employing the rheology equation (5) above, transitions from mobile- to SLC are determined by systematically increasing the viscosity contrast parameter γ (beginning with an isoviscous case) while keeping the value of f fixed. A critical viscosity contrast $\Delta\eta_{\mathrm{SLC}}$ is determined that marks the onset of SLC for various curvatures. The range of curvatures tested generally includes $f = 0.3$, 0.4, 0.5, 0.55, 0.7, and 0.9 (thus sampling the geometries of the silicate mantles of dwarf planets, Earth-like bodies, and the thin outer shells of icy moons). In addition, we compare findings to aspect ratio 10 two-dimensional Cartesian geometry calculations. The viscosity contrasts considered range between 1 and 10^8 where 1 represents the isoviscous case.

3. Results

We first consider convection in a 2-D spherical annulus and aspect ratio 10 Cartesian geometries. Here we isolate the effect of core surface area on convective regimes. The degree of system curvature increases as f decreases. In general, we focus on systems where $f = 0.3$, 0.4, 0.5, 0.7, and 0.9. Several calculations characterized by $f = 0.2$ are also included to illustrate the peculiarities of small-core systems.

In the accompanying supporting information document, we present all tables referred to in section 3 followed by a selection of resolution-test examples.

3.1. Influence of Core-Size on the Convective Regime and Temperature

In Figure 1, we plot temperature field snapshots for calculations featuring different f and $\Delta\eta_T$ values. (The notation log denotes a base 10 logarithm in all figures of this paper unless stated otherwise.) These snapshots show the effect that viscosity contrast has on flow pattern and convective regime as a function of system geometry and the range of behavior possible within the regimes defined. In Figure 1a flow patterns corresponding to examples of the transitional regime ($0.01 < M < 1.0$) in Cartesian geometry drastically contrast between a flow featuring robust large downwelling sheets ($M = 0.73$ and $\Delta\eta_T = 10^3$) and a system with a hot convective interior and a sluggish lid ($M = 0.04$ and $\Delta\eta_T = 10^5$). The stagnant-lid regime is well established with $\Delta\eta_T = 10^7$ (i.e., $M = 10^{-4}$) and is characterized by a hot convective interior featuring drip-like

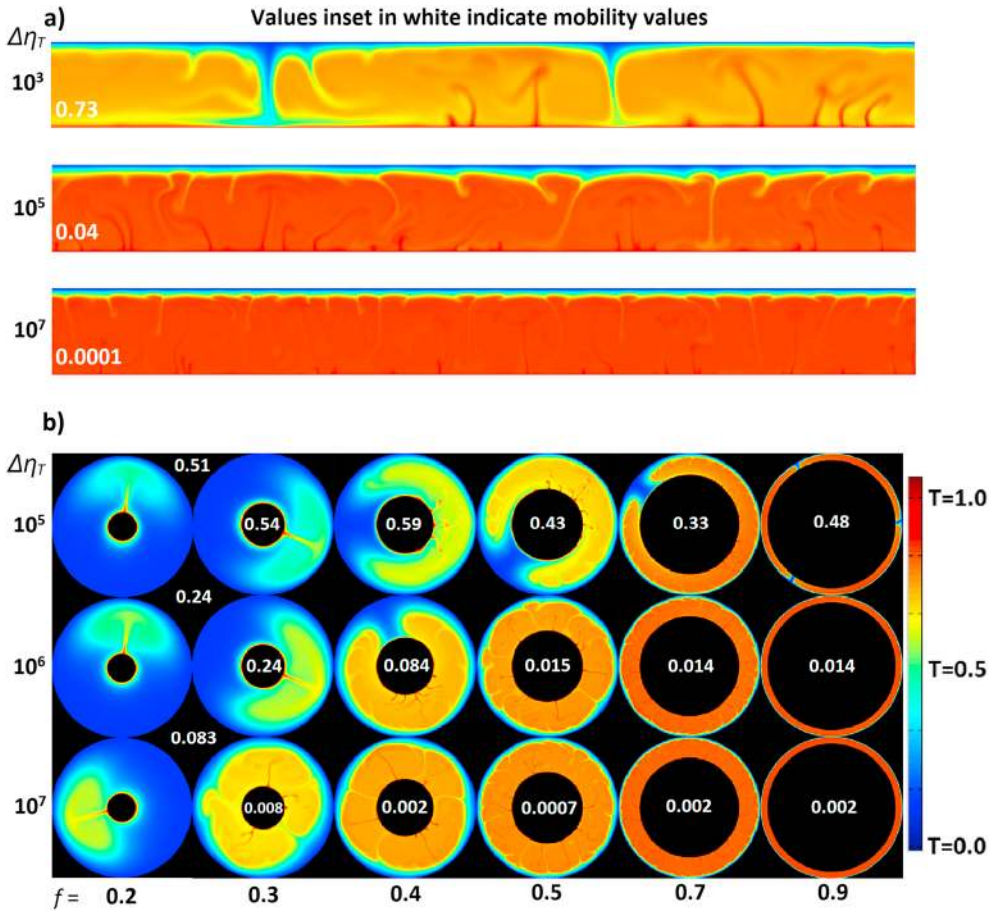

Figure 1. Selected nondimensional temperature field snapshots for Cartesian and spherical geometries with purely basal heating. (a) Temperature fields in an aspect ratio 10 geometry with $\log(\Delta\eta_T) = 3, 5$, and 7 from top to bottom, respectively. (b) Temperature fields for convection in spherical annuli with $f = 0.2, 0.3, 0.4, 0.5, 0.7$, and 0.9 from left to right and $\log(\Delta\eta_T) = 5, 6$, and 7 (log base 10) from top to bottom, respectively. The temperature for all snapshots correspond to the color bar. Mobility values for all cases are inset.

downwellings at the base of a conductive lid. In the first row of Figure 1b, for all f values, spherical annulus convection with fixed viscosity contrast $\Delta\eta_T = 10^5$ and increasing core size satisfies the mobility condition of the transitional regime ($0.01 < M < 1.0$). The temperature field plots reveal a fundamentally different flow in the spherical geometry models in comparison to the Cartesian geometry case with the same parameters (Figure 1a, middle panel). When $f \leq 0.7$, a hemispherical dichotomy develops characterized by hot upwellings that are dominant in one hemisphere and a large downwelling in the opposite hemisphere. When $f = 0.9$, distinct hemispheres are no longer found. Given that the annuli are solutions in the equatorial cross section of a spherical shell with no variation in colatitude, upwelling and downwelling features in the 2-D solutions can be thought of as a crescent-like sheet of maximum thickness in the equatorial plane that tapers until vanishing at the poles of the sphere. (That is, in a spherical geometry where the colatitude $\theta = \pi/2$ coincides with the plane of the annulus; a 3-D spherical harmonic decomposition of the solution obtained would have only sectoral harmonics, analogous to the segments in an orange.) The volume of the downwelling depends on the viscosity contrast and decreases as $\Delta\eta_T$ increases. The onset of SLC, hereafter referred to as SLC occurs with the elimination of the cold (blue) downwelling. In the second row of Figure 1b, the small core ($f \leq 0.4$) cases are convecting with a sluggish-lid character and each system is at the threshold of SLC. In the final row of Figure 1b ($\Delta\eta_T = 10^7$), SLC occurs for all curvatures except the $f = 0.2$ case. However, even when a stagnant-lid is present, as f decreases mean temperature decreases so that upwelling strength increases. Thus, when f is small, SLC is obtained with distinct upwellings and a thermal boundary layer above the core.

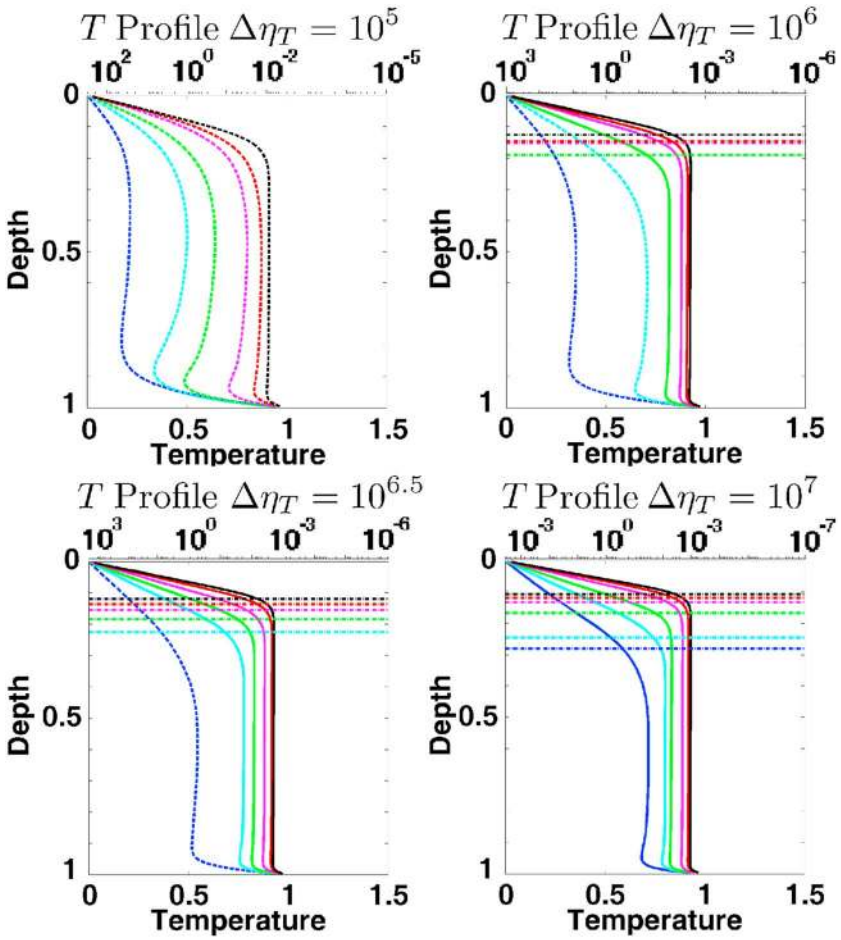

Figure 2. Horizontally averaged temperature profiles for selected viscosity contrasts. Curvature is represented by the color scheme: $f = 0.3$ (blue), $f = 0.4$ (cyan), $f = 0.5$ (green), $f = 0.7$ (magenta), $f = 0.9$ (red), and $f = 1.0$ (black). Convective regimes are denoted by dashed lines (transitional) and solid lines (stagnant lid) and the horizontal dot-dashed lines mark the base of the conductive stagnant lid.

Figure 2 shows temporally averaged temperature profiles for selected thermal viscosity contrasts. Due to the high viscosity contrasts required to obtain SLC when $f = 0.2$, we generally analyze behavior when $f \geq 0.3$ and present only select cases for $f = 0.2$. Transitional regime cases are denoted by dashed curves and SLC is denoted by solid curves (as determined by the mobility criterion). In each stagnant-lid case, the base of the conductive lid is marked by a horizontal dot-dashed line; the depth of the lid is calculated by finding the y intercept of the line tangent to the inflection point on the profile of the vertically advected heat (Davaille & Jaupart, 1993). In the stagnant-lid regime, the upper thermal boundary becomes thinner as curvature decreases (i.e., f increases).

Due to the asymmetry in the areas of the heating and cooling surfaces, in isoviscous convection the temperature gradient across the upper thermal boundary layer decreases as f is decreased (e.g., Vangelov & Jarvis, 1994). In convection with a strongly temperature-dependent viscosity, as curvature increases the temperature change across the stagnant lid is reduced for the same reason. Thus, a higher viscosity contrast is required to obtain the same viscosity increase across the conducting lid. Moreover, the temperature of the deep interior (i.e., middepth) is closer to the reference temperature when f is smaller so that the viscosity increase across the upper thermal boundary layer is much less than in higher f geometries. For example, Figure 2 shows that when $f = 0.3$ and $\Delta\eta_T = 10^{6.5}$ the difference in viscosity between the surface and the top of the lower thermal boundary layer is approximately $(\Delta\eta_T)^{1/2}$. However, for $f > 0.5$ similar behavior is not observed in any cases. In summary, the viscosity contrast across the upper thermal boundary layer must be increased by increasing the global viscosity contrast, in order to obtain the contrast required across the upper thermal boundary layer that allows for decoupling of the conductive lid and convecting interior. An additional consequence

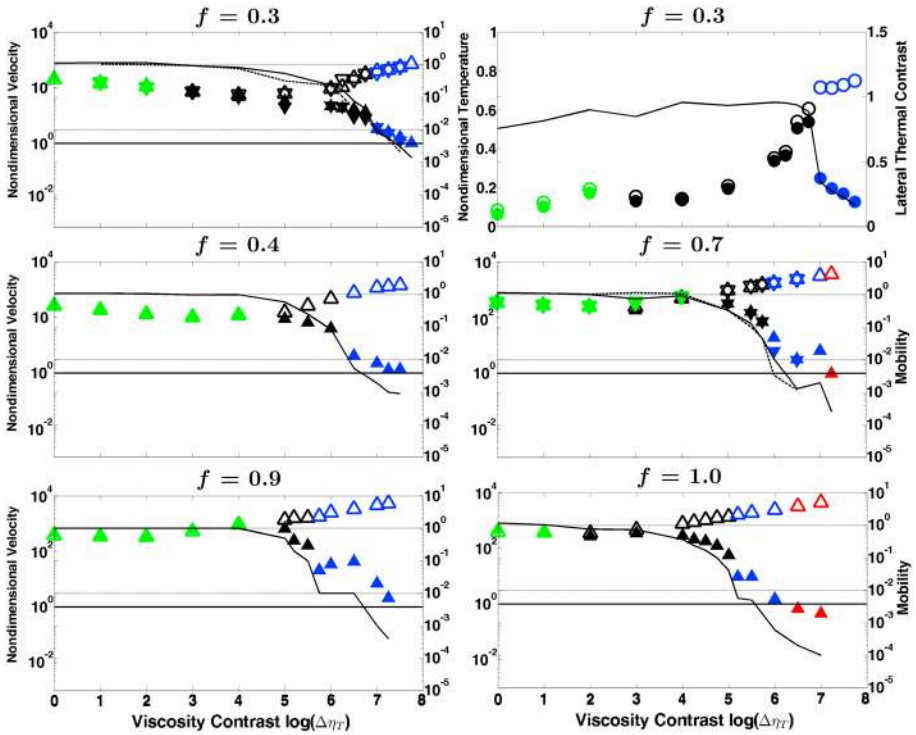

Figure 3. All panels except the upper right show mobility (solid curve, right-hand scale), volume-averaged rms velocity (open triangles, left-hand scale) and surface rms velocity (closed triangles, left-hand scale) as a function of thermal viscosity contrast for systems with different curvature, f. Triangles with a vertex at the top indicate that for the associated datum point, viscosity was increased relative to the field used to obtain the initial condition, and triangles with a vertex at the bottom (i.e., pointing down) indicate that viscosity was decreased relative to the field used to obtain the initial condition. In the $f = 0.3$ and $f = 0.7$ cases, data are presented for two suites of calculations, one where viscosity is systematically increased and the other where it is decreased. In the latter case mobility is plot with a dashed curve. (For other f values, the only cases plotted correspond to viscosity contrast being increased.) In the upper right panel, open circles denote time averaged middepth temperatures, closed circles denote the temperature difference between the hottest and coldest regions at middepth and the solid black curve denotes the ratio of the lateral thermal contrast difference to the average (only the cases where viscosity is being increased are plotted). All calculations feature $\mathrm{Ra}((T^* - T_{\mathrm{surf}})/\Delta T = 0.5) = 3.2 \times 10^5$. Green symbols denote cases with $M > 1.0$ (mobile lid), black symbols with $0.01 < M < 1.0$ (transitional), blue symbols with $M < 0.01$, and red symbols denote $M < 0.01$ and $V_{\mathrm{surf}} < 1$ (stagnant lid). The upper horizontal dotted line denotes $M = 1.0$, the lower horizontal dotted line denotes $M = 0.01$ and the solid horizontal line denotes $V_{\mathrm{surf}} = 1$.

of the effect of curvature on producing a cooler global mean temperature occurs below the conducting lid. Using the thickness of the conductive lid as a reference for determining the thickness of the convecting layer, the viscosity variation across the latter, $\Delta\eta_{\mathrm{CL}}$, is seen to increase as curvature increases.

For the highest viscosity contrast examined, the intersection of the temperature profiles and the dashed lines in Figure 2 show that the viscosity contrast across the convective layer remains below 10^2 except for in the highest curvature case ($f = 0.3$) where temperature variation across the convecting layer is greater than 0.4 and viscosity variation is almost 3 orders of magnitude. For larger f SLC cases, once viscosity contrasts exceed $\Delta\eta_T = 10^6$ further increases only add to the contrast across the stagnant lid. These findings are consistent with the analysis presented by Yao et al. (2014) that implies the convective layer is almost isoviscous regardless of the value γ once SLC is obtained (Davaille & Jaupart, 1993; Solomatov, 1995). However, with $f < 0.5$ the convective layer features larger $\Delta\eta_{\mathrm{CL}}$ and greater sensitivity of $\Delta\eta_{\mathrm{CL}}$ to γ.

Figure 3 plots mobility, volume-averaged velocity and surface rms velocity versus the magnitude of the viscosity contrast $\Delta\eta_T$ for varying curvature f. For the case $f = 0.3$, the upper right panel of Figure 3 shows the onset of an increase in mean temperature of the system interior, as well as temperature contrasts, as M drops below 1.0 (upper left panel). In particular, the thermal field transitions between end-member states characteristic of the mobile and stagnant-lid regimes, while mobility drops by approximately 2 orders of magnitude. Comparing the $f = 0.3$ and $f = 1.0$ cases shows that the thermal viscosity contrast required for the onset of SLC

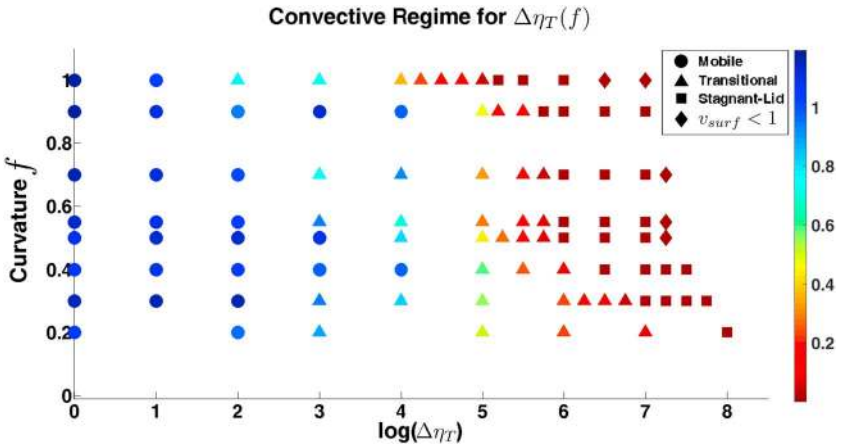

Figure 4. Convective regimes for purely basally heated calculations are plotted as a function of curvature f and logarithm of the thermal viscosity contrast $\log(\Delta\eta_T)$. Color indicates the temporally averaged mobility of the indicated case. To emphasize the onset of stagnant-lid convection symbols are used to indicate convective regime by rounding the mobility values to a single digit. Circles correspond to mobile regime ($M \geq 1.0$), squares correspond to stagnant-lid cases ($M < 0.01$), and triangles correspond to transitional cases. Diamonds represent stagnant-lid convection with $M < 0.01$ and $V_{surf} < 1$. Mobility values for all cases represented in this figure are listed in the supporting information (Tables S1–S3).

at this Ra differs by an order of magnitude. Specifically, if only the mobility criterion is considered the onset of SLC is obtained with $\Delta\eta_T \approx 10^7$ for $f = 0.3$ and $\Delta\eta_T \approx 10^6$ for $f = 0.7$. Augmenting the mobility criterion with the stricter surface velocity condition, $V_{surf} < 1$ (Stein et al., 2013), we find the contrast required for the onset of SLC is increased. For a Cartesian geometry, the onset of SLC occurs for a lower viscosity contrast with $\Delta\eta_T \approx 10^{5.5}$ (and $\Delta\eta_T \geq 10^6$ when $V_{surf} < 1$). For each core size, the decreasing values in mobility result from a decreasing surface velocity and corresponding increase in interior velocity. The latter effect occurs as viscosity drops with the global temperature increase that accompanies the decrease in surface velocity. When the temperature below the stagnant-lid increases above the reference temperature, the Rayleigh number increases above the reference value and the convection becomes characterized by a V_{rms} that is increased relative to the isoviscous case. The onset of SLC (defined by a critical value of $\Delta\eta_T$ as a function of f, $\Delta\eta_{SLC}$) follows a monotonically decreasing but nonlinear trend in $f - \log(\Delta\eta_T)$ space (discussed further in section 5.2).

In the panels corresponding to $f = 0.3$ and 0.7 in Figure 3 data are plotted for two suites of calculations. In the first case (the case used for all geometries) each experiment uses a solution corresponding to the next lowest viscosity contrast as the initial condition, starting from the isoviscous solution that is obtained from a randomly perturbed conductive field. In the second suite, a stagnant-lid solution is the starting initial condition and viscosity is systematically decreased (further information is given in the figure caption). For the two geometries examined we generally find convergence of the solutions (yielding a six-vertex star) for a given viscosity contrast for each of the initial conditions but with minor differences. Where the solutions differ more substantially we find that the difference is explained by the number of convection cells in the final state. We discuss this further in section 3.3.

Figure 4 summarizes convective regime as a function of logarithm of thermal viscosity contrast, for varying curvature f when $\mathrm{Ra} = 3.2 \times 10^5$. Color indicates the temporally averaged mobility of the cases shown. The onset of SLC determined by a mobility criterion alone ($M < 0.01$) is shown by square symbols. As f decreases the viscosity contrast required to reach the stagnant-lid regime increases. An irregular trend in the circles and triangles (i.e., nonmonotonic increase in $\Delta\eta_T$ with f) occurs due to variation in the number of convection cells (discussed further in section 3.3).

In addition to convective regime, middepth temperature changes substantially as a function of the $\log(\Delta\eta_T)$ for different geometries. Temperatures increase by more than a factor of 4 for $f = 0.3$ versus $f = 0.9$ when $\Delta\eta_T = 10^5$ (for convection in the transitional regime). When $\Delta\eta_T = 10^7$ all geometries (except $f = 0.2$) exhibit SLC, but interior temperatures in $f = 0.9$ and Cartesian geometries are more than 30% above the temperature in a $f = 0.3$ case. Prior to the onset of SLC, temperature is strongly dependent on the number of downwellings present. In this context, the downwellings we refer to feature cold fluid sourced from the upper

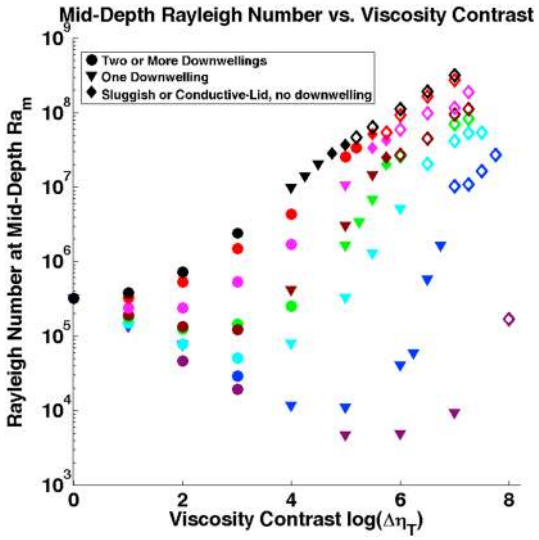

Figure 5. Middepth Rayleigh number as a function of viscosity contrast. Curvature is represented by the color scheme: $f = 0.2$ (purple), $f = 0.3$ (blue), $f = 0.4$ (cyan), $f = 0.5$ (green), $f = 0.55$ (brown), $f = 0.7$ (magenta), $f = 0.9$ (red), and $f = 1.0$ (black). The inset defines the correspondence between symbols and the number of downwelling observed in the case reported, where the term downwelling refers to cold fluid sourced from the upper thermal boundary layer sinking deep into the convecting system (for example, see Figure 1). Open symbols indicate stagnant-lid convection.

thermal boundary layer, which participates in the convection. We find that in the transitional regime, single downwellings dominate when $f \leq 0.55$. For isoviscous shells with this curvature, Jarvis et al. (1995) noted a fundamental change to single plume convective planform when $f \leq 0.5$. The cooler mean temperatures of small-core systems result in higher mean viscosities and lower effective Rayleigh numbers. The potential for generating instabilities, producing multiple upwellings, warmer interiors, and higher effective Rayleigh numbers is greater for shells with large cores, due to the greater heat input delivered per unit volume of convecting fluid by a larger basal heating surface.

3.2. The Effect of T^*

Given a viscosity that decreases with increasing temperature, and a nondimensional reference temperature equal to 0.5, there is a fundamental difference between basally heated Cartesian geometry and spherical shell convection. When γ is increased beyond an isoviscous starting point (i.e., $\gamma = 0$), mean system viscosity decreases monotonically in the former case, while increasing until a local maximum is reached in the latter geometry (before decreasing). Equivalently, in a spherical shell the effective Rayleigh number first decreases as $\Delta\eta_T$ is increased from the isoviscous state. For any f value, this same behavior will cause convection to eventually cease if T^* is set equal to the CMB temperature and γ is systematically increased. In a spherical shell system T^* should be set to, at most, the mean temperature characterizing isoviscous convection, in order to obtain an increase in the effective Rayleigh number as $\Delta\eta_T$ is increased relative to the isoviscous state.

This effect is illustrated with system results that are analyzed by plotting convective vigor (effective Rayleigh number at middepth) against the viscosity contrast (Figure 5). The Rayleigh numbers, $\mathrm{Ra_m}$, were calculated by taking the time averaged temperature at middepth and applying equation (7). For all curvatures, the middepth Ra is 3.2×10^5 in the isoviscous case. However, middepth temperatures are increasingly cooler as f decreases. Accordingly, for cases with curvature $f < 1$ convective vigor first decreases with increasing viscosity contrast, eventually reaching a minimum value. The minimum value increases with increasing curvature (decreasing f). When $f = 0.3$, as $\Delta\eta_T$ is increased (e.g., when $\Delta\eta_T = 10^5$), the middepth Rayleigh number, $\mathrm{Ra_m}$, drops by more than 3 orders of magnitude relative to the Cartesian case and a factor of 30 relative to the isoviscous case. When $f = 0.2$ and $\Delta\eta_T = 10^7$ the $\mathrm{Ra_m}$ has dropped by approximately a factor of 50 relative to the isoviscous case while all other cases have converged to the stagnant-lid regime with $\mathrm{Ra_m}$ at least a factor of 50 greater than in the isoviscous case.

By adopting a value for $T^* - T_{\mathrm{surf}}$ of $0.5\Delta T$, at first equation (5) appears to be preferentially tailored to modeling Cartesian geometry systems. For example, as noted above when $T^* - T_{\mathrm{surf}} = 0.5\Delta T$ it is only for this geometry that Rayleigh number is not effectively lowered as $\Delta\eta_T$ is first increased. The change in mean temperature that occurs with f (e.g., in isoviscous convection) therefore suggests that it may be appropriate to change the reference temperature T^* to account for geometry so that transitions, say to the stagnant-lid regime, will occur for the same viscosity contrast in different geometries. However, the rheology modeled by equation (5) does not make T^* an independent parameter from Ra. For example, if we set $T^* = T_{\mathrm{surf}} + 0.17\Delta T$ (the mean of the conductive temperature profile in an $f = 0.3$ spherical shell) then a much larger volume of the shell will feature nondimensional viscosities less than 1.0 (thus raising the effective Rayleigh number). Mathematically, this is equivalent to holding T^* equal to $T_{\mathrm{surf}} + 0.5\Delta T$ and increasing the Ra by a factor of $(\Delta\eta_T)^{0.5-0.17} = (\Delta\eta_T)^{0.33}$ (which is equal to 20.9 for $\Delta\eta_T = 10^4$) because equation (5) can be written

$$\eta(T) = \eta^* \exp(-\gamma((T - T_{\mathrm{surf}})/(\Delta T) - 0.17)) = \eta^* \exp(-0.33\gamma) \exp(-\gamma((T - T_{\mathrm{surf}})/(\Delta T) - 0.5)), \quad (8)$$

that is,

$$\eta(T) = \eta^* (\Delta\eta_T)^{-0.33} \exp(-\gamma((T - (T_{\mathrm{surf}} + 0.5\Delta T))/\Delta T)). \quad (9)$$

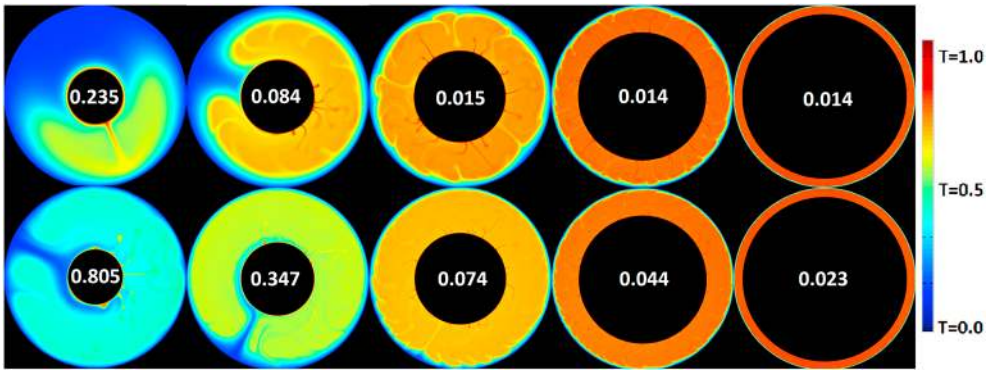

Figure 6. Nondimensional temperature field snapshots for basally heated spherical annulus models with $(T^* - T_{surf})/\Delta T = 0.5$ (top row) and $T^* - T_{surf} = T_{cond}$ (bottom row). Each system has a viscosity contrast $\Delta\eta_T = 10^6$. $T_{cond}(f = 0.3) = 0.17\Delta T$, $T_{cond}(f = 0.4) = 0.23\Delta T$, $T_{cond}(f = 0.5) = 0.29\Delta T$, $T_{cond}(f = 0.7) = 0.38\Delta T$ and $T_{cond}(f = 0.9) = 0.46\Delta T$ (left to right, respectively). Mobility values are inset.

Accordingly, changing the reference temperature from T_i to T_f yields the same system as changing the reference Ra to $(\Delta\eta_T)^{(T_i - T_f)/\Delta T}$Ra while leaving the reference temperature as T_i.

In Figure 6 we present temperature field snapshots from calculations in which T^* is set equal to the mean of the conductive temperature profiles for cases with various geometries. When $\Delta\eta_T = 10^6$ the changes in T^* are equivalent to multiplying the Rayleigh numbers by 95.5 ($f = 0.3$), 41.7 (f=0.4), 18.2 ($f = 0.5$), 5.2 ($f = 0.7$), and 1.74 ($f = 0.9$) in comparison to cases where $T^* - T_{surf} = 0.5\Delta T$. We limit the remainder of the study of the role of f to cases where we vary only γ with a fixed Rayleigh number and $T^* = 0.5\Delta T + T_{surf}$ (with an understanding that variation of T^* is equivalent to varying Ra).

3.3. Discontinuities and Anomalies in the Onset of Convective Regimes

In Figure 4, an apparent discontinuity (or at least a very high gradient) is observed for the onset of the transitional convective regime between systems with zero ($f = 1.0$) and low curvature ($f = 0.9$). The change to convection in the transitional regime occurs with a viscosity contrast of $\Delta\eta_T = 10^5$ for each spherical system examined whereas (for the aspect ratio 10 calculations we examined) Cartesian geometry convection transitions with $\Delta\eta_T = 10^2$. Transitional regimes are characterized by downwelling/upwelling sheets in 2-D Cartesian geometry versus sectoral-harmonic "segments" in 2-D spherical annulus systems. The fundamental difference in the topology of the systems may explain the disparity in the required $\Delta\eta_T$ for the onset of the transitional regime.

Figure 5 shows that a transition to a single downwelling flow pattern typically precedes the onset of SLC as $\Delta\eta_T$ is increased. For the Rayleigh number specified here, prior to the transition to SLC, flow characterized by a single downwelling appears to be a robust feature for curvatures with $f \leq 0.7$. Moreover, single downwellings are obtainable in our $f = 1.0$ calculations as convection cell widths do not need to exceed an aspect ratio of 5 (similar to the cell widths found with a single downwelling when $f \sim 0.50$). However, when curvatures are small ($f \geq 0.9$) single downwelling flow is difficult to achieve because extremely long wavelength convection cells must be generated. Consistent with this observation, it appears that the onset of transitional surface mobility is delayed when long aspect ratio cells are obtainable. The aspect ratio 10 limit when $f = 1.0$ may thus be an alternative explanation for the discontinuity in Figure 4 (between $f = 0.9$ and 1.0 transitional regime onset).

Figure 7 compares $f = 0.5$ and $f = 0.7$ spherical annulus cases featuring viscosity contrasts increasing from 10^2 to 10^6. In the top two rows, for each adjacent pair the solution to the right is obtained starting from the field to the left. In the bottom row, the solution to the left is obtained starting from the field to the right. When $f = 0.5$, the number of convection cells decreases from four to a pair before the onset of SLC as $\Delta\eta_T$ is increased, and mobility decreases smoothly from left to right in the figure. In contrast, when $f = 0.7$ and viscosity contrast is systematically increased, the number of convection cells changes sharply between the $\Delta\eta_T = 10^3$ and 10^4 cases and mobility increases before starting a monotonic decrease as $\Delta\eta_T$ is increased further (see Figures 3 and 4). Similar behavior also occurs as viscosity contrast is decreased systematically (bottom row) as mobility drops when four cells are superseded by multiple cells with a decrease in viscosity

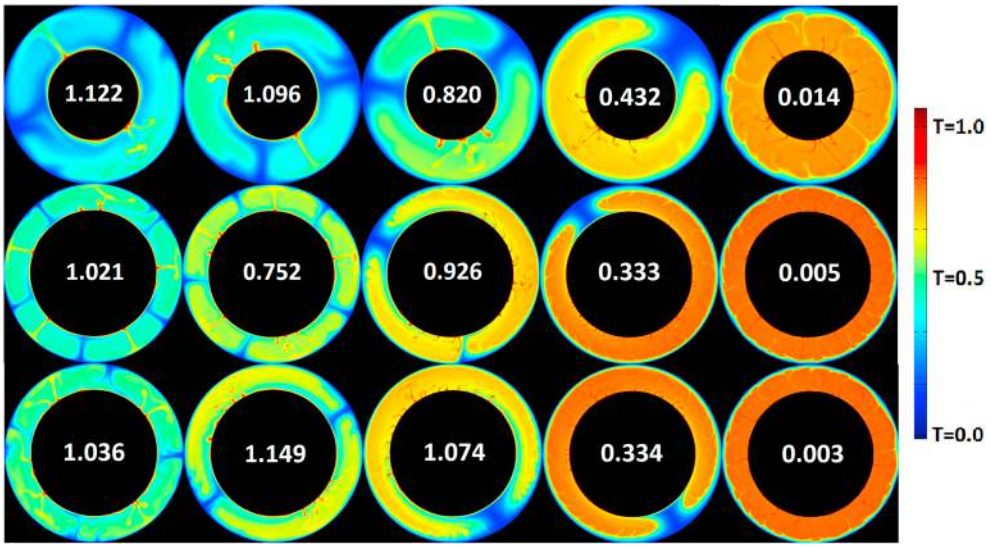

Figure 7. Temperature field snapshots featuring $\Delta\eta_T = 10^2, 10^3, 10^4, 10^5$, and 10^6 (left to right) for $f = 0.5$ (top) and $f = 0.7$ (bottom two rows) curvatures. Mobility values are inset. In the top two rows, solutions are obtained from an initial condition field with a factor of 10 lower total viscosity contrast. In the bottom row, solutions are obtained from an initial condition with a factor of 10 higher total viscosity contrast (i.e., for each adjacent pair, the solution to the left is obtained starting from the field to the right).

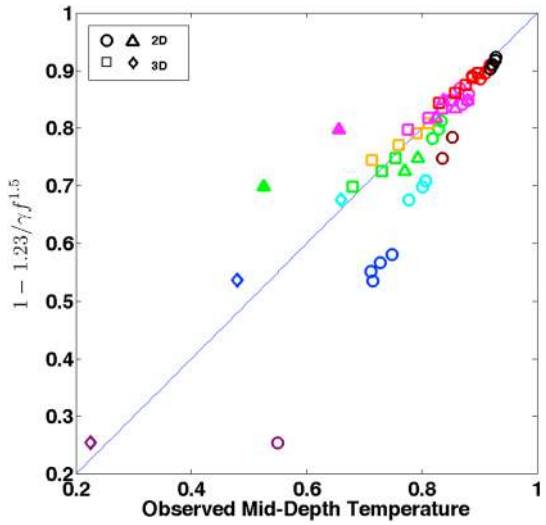

Figure 8. Observed middepth temperatures for basally heated stagnant-lid convection calculations are plotted against predicted temperatures using the equation for average temperature in the well-mixed interior below a stagnant lid, $(T_m - T_{surf})/\Delta T$, determined by Yao et al. (2014). Open squares represent the 3-D cases analyzed by Yao et al. (2014). The open circles represent 2-D cases from this study with $Ra = 3.2 \times 10^5$. Triangles represent our findings for 2-D calculations with the same parameters as cases marked by open squares. Open triangles represent stagnant-lid convection and solid triangles represent transitional convection. Open diamonds represent 3-D stagnant-lid convection cases for $f = 0.2(\Delta\eta_T = 10^8)$, $f = 0.3(\Delta\eta_T = 10^7)$, and $f = 0.4(\Delta\eta_T = 10^{6.5})$. Curvature is represented by the color scheme: $f = 0.2$ (purple), $f = 0.3$ (blue), $f = 0.4$ (cyan), $f = 0.5$ (green), $f = 0.55$ (brown), $f = 0.6$ (orange), $f = 0.7$ (magenta), $f = 0.9$ (red), and $f = 1.0$ (black).

contrast from 10^3 to 10^2. Generally, system mobility decreases monotonically as $\Delta\eta_T$ is increased when the number of convection cells does not change, but trends can change when the downwelling number changes with increasing (or decreasing) viscosity contrast.

Figure 7 also shows that different steady convective patterns are obtainable for the same set of system parameters and that the cell number is dependent on the initial condition. Moreover, the time-dependent averaging of the mobility calculated may yield some differences in values for seemingly identical solutions (e.g., $f = 0.7$ cases with viscosity contrasts of 10^5 and 10^6). However, we did not find examples of the same set of parameters yielding SLC for one initial condition versus transitional or mobile-lid convection for a different initial condition. (Such behavior, commonly termed "hysteresis," has been widely observed in systems that include stress-dependent viscosities (e.g., O'Neill et al., 2016; Weller & Lenardic, 2012).)

4. Comparison Between 2-D and 3-D Systems

Figure 8 plots observed middepth temperatures for calculations of SLC against the mean temperatures below the stagnant lid predicted by the analysis of Yao et al. (2014). The colors correspond to specific f values as in Figure 5 and $T^* - T_{surf} = 0.5\Delta T$ in all cases. The square symbols represent the 3-D spherical shell stagnant-lid cases reported by Yao et al. (2014), and the triangles represent 2-D spherical annulus calculations featuring the same parameters as the cases corresponding to the squares (Ra varies). Open triangles represent SLC and solid triangles represent transitional convection. The circles plot all of the spherical annulus stagnant-lid cases in our study featuring $Ra = 3.2 \times 10^5$. (In the Yao et al. (2014) study, stagnant-lid cases were not found for small-core systems [e.g., $f \leq 0.4$].) The diamonds correspond to three cases of SLC in 3-D spherical shells featuring the same parameters as spherical annulus cases presented earlier

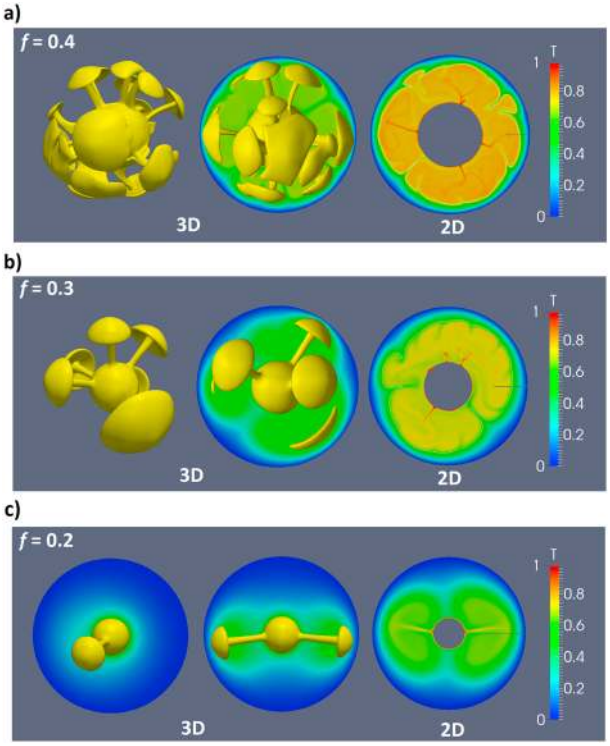

Figure 9. Two-dimensional and 3-D nondimensional temperature field snapshots comparing stagnant-lid convection in small-core spherical geometries. Panels show (a) $f = 0.4$, (b) $f = 0.3$, and (c) $f = 0.2$ spherical systems. Model parameters are identical in each panel, only the dimensionality differs. For (a) and (b) the left-hand column shows $(T - T_{surf})/\Delta T = 0.7$ and 0.6 isosurfaces, respectively, corresponding to hot upwellings. For (c) the left-hand column shows the $(T - T_{surf})/\Delta T = 0.6$ isosurface superimposed on a vertical slice through the spherical shell. For all panels the center column shows the same isosurfaces but from a viewing angle rotated by 90° in the equatorial plane, relative to the viewing angle in the left column. The isosurfaces are superimposed on a vertical slice through the spherical shell. The right-hand column shows a spherical annulus centered at the equator. The grid dimensions in the 3-D cases are $2 \times (128 \times 384 \times 64)$ and in the 2-D case $1,024 \times 64$ (for $f = 0.3$ and $f = 0.2$) and $1,280 \times 64$ (for $f = 0.4$).

in this paper. Observed lowest temperature cases for $f = 0.5$ (green) and $f = 0.7$ (magenta) are much colder for the coldest 2-D case when compared with the 3-D cases and correspond to the lowest viscosity contrast investigated in this study. The anomalous temperatures occur because the 2-D calculations do not feature stagnant lids for the specified parameters. Thus, the onset of SLC occurs for smaller $\Delta\eta_T$ values in 3-D. However, we find that when SLC occurs in a spherical annulus geometry it generally results in hotter solutions when compared to convection in spherical shells and that the disagreement increases as f decreases. In addition, we find that when $f \leq 0.3$ our 3-D spherical shell calculation does not agree as well with the trend found by Yao et al. (2014). Given that only spherical shells with $f \geq 0.5$ were used to obtain the equation for predicted temperatures in the study by Yao et al. (2014), it is not inconsistent to find that small-core cases are less well fit by this equation. Moreover, the parameterizations given by Yao et al. (2014) assumed that the convection below the stagnant lid is essentially isoviscous. Our findings (Figure 2) show that this assumption breaks down when $f \leq 0.4$.

Figure 9 shows details in the difference between 2-D spherical annulus and 3-D spherical shell convection for cases where $f = 0.4$ with $\Delta\eta_T = 10^{6.5}$, $f = 0.3$ with $\Delta\eta_T = 10^7$, and $f = 0.2$ with $\Delta\eta_T = 10^8$. In each panel, the spherical annulus case is on the right. In their study, Yao et al. (2014) only found weak convection with single plume flow and thick thermal boundary layers in small-core geometries. Figure 5 clarifies that this is because effective Ra is lowered by increasing γ with $T^* - T_{surf} = 0.5\Delta T$ and that Yao et al. (2014) would have needed to examine much larger Ra and $\Delta\eta_T$ cases in order to obtain stagnant lids with $f \leq 0.4$. Flow patterns in the spherical shell calculations are characterized by multiple plumes and a robust stagnant lid. The stagnant lid is depicted as a blue layer in the equatorial slice, and the convective interior appears to be an almost uniform temperature. In contrast to SLC in a Cartesian geometry system, these examples of SLC with relatively small cores feature thermal boundary layers at the core mantle boundary and hot plumes relative to the ambient mantle. The spherical annulus case is hotter in each small-core geometry, but the temperature field snapshots indicate similar separation distances between the active upwellings in each geometry. Temperature differences are likely explained by the topological difference between flows in a spherical shell and spherical annulus. Upwellings obtained in spherical annulus geometries model sectoral sheets that terminate at the poles of the sphere (normal to the plane in which the field is calculated). A 3-D spherical shell calculation features columnar plumes. This difference is especially illustrated in the $f = 0.2$ case where hot upwelling regions fill over 50% of the interior at all latitudes in a 2-D model. In contrast, the two hot plumes in the 3-D case can occupy a smaller volume of the shell. In Figure 9c a slice perpendicular to the plane featuring the two plumes is very low in temperature. No such slice exists through the annulus topology. It appears that the impact of this difference on temperature, corresponding to a planform difference, becomes amplified as f decreases. Previously, for isoviscous convection, Shahnas et al. (2008) noted that planform variations affect mean temperature so that convection with plumes and sheets do not follow the same parameterizations.

5. Discussion

5.1. Implications for Modeling

The thermal parameterization for SLC derived by Yao et al. (2014) for 3-D calculations implies that SLC features a conductive thermal upper boundary layer atop an almost isoviscous convecting layer (i.e., the thermal viscosity $\Delta\eta_{CL} \lesssim O(10)$). Making this assumption for larger values of f (> 0.5), it follows that

$$1 - \left(\frac{T_m - T_{surf}}{\Delta T}\right) = \delta/(\gamma f^{\beta}). \tag{10}$$

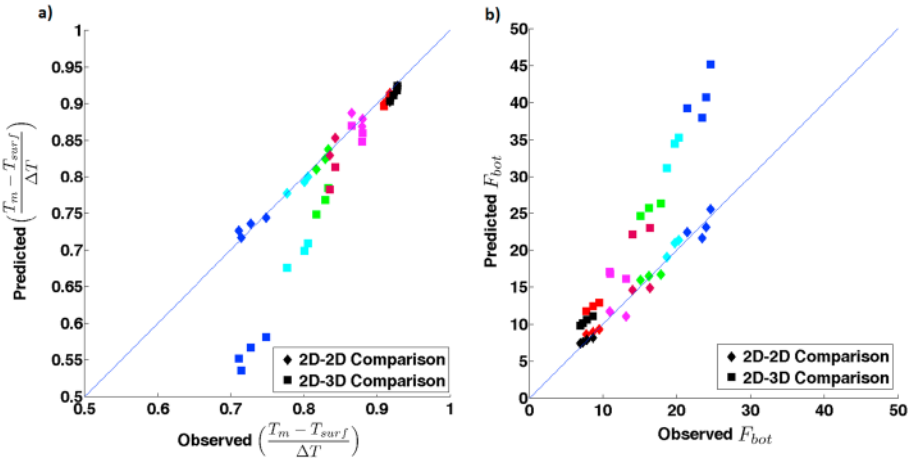

Figure 10. Observed (a) middepth temperature and (b) basal heat flux for stagnant-lid convection in basally heated calculations, plotted against parameterized values. Solid squares plot 2-D observations against values predicted by an equation based on 3-D findings derived by Yao et al. (2014). Solid diamonds plot the 2-D observations from this study against the middepth temperature equation (10) and basal heat flux equation (11) obtained using the 2-D results. Color corresponds to curvature as in Figure 8.

Yao et al. (2014) fit their results to find that $\delta = 1.23 \pm 0.15$ and $\beta = 1.5 \pm 0.22$. Using the results of our 2-D calculations, we solved equation (10) for best fit keeping the coefficient δ fixed at 1.23 and found $\beta = 1.09 \pm 0.01$. Note that the parameter δ is fixed so that the power-law dependence of our 2-D results can be compared specifically with the exponential dependence derived by Yao et al. (2014) for fully 3-D results and so that the equations converge for plane-layer geometries. For a viscosity contrast determined by γ, in 2-D, the drop in nondimensional temperature across the lower thermal boundary layer (left side of (10) is reduced compared to the finding based on 3-D geometry calculations due to the reduced value of β. That is, annuli interiors are always hotter than their 3-D counterparts in the SLC regime.

With the temperature jump across the lower thermal boundary layer given by the right side of 10, basal heat flux is given by

$$F_{\text{bot}} = a\text{Ra}_{\text{m}}^{b}/(\gamma^{c} f^{d}). \tag{11}$$

Yao et al. (2014) found $a = 2.01 \pm 0.26$, $b = 0.30 \pm 0.01$, $c = 1.50 \pm 0.01$, and $d = 1.91 \pm 0.03$. Using results from the 2-D calculations and keeping a and b fixed, we obtain $c = 1.61 \pm 0.02$ and $d = 1.70 \pm 0.05$ in equation (11). Again, we choose to fix a and b to isolate the power-law dependence of basal heat flux on the effect of viscosity contrast and curvature in 2-D annulus versus 3-D systems (Yao et al., 2014).

The left panel in Figure 10 plots the observed middepth temperature from the spherical annulus calculations against the temperature drop determined with equation (10) for values of β obtained using both 2-D and 3-D calculations. The right panel of Figure 10 plots the basal heat flux against the heat flux predicted with equation (11) where c and d determined from both the 2-D and 3-D studies are utilized. As curvature is increased, observed values for $(T_{\text{m}} - T_{\text{surf}})/\Delta T$ and F_{bot} in annuli differ greatly from those calculated using Yao et al.'s (2014) equation with exponents based on fitting results from 3-D spherical shells. Consistent with the trend of the temperature drops exhibited in panel a, the basal heat fluxes observed are lower in the annuli calculations and the disagreement between 2-D and 3-D systems increases as f decreases. Although the 2-D parameterization is successful, we find that the parameterization of the 2-D results is poorest for thin shells.

In Figure 11a we plot predicted temperature drop across the basal boundary layer as a function of f using equation (10) with β determined from both 2-D and 3-D calculations. Open diamonds plot the observed temperature drop as a function of f and show that the 2-D parameterization works well in general but is less successful for the $f = 0.9$ case. The solid diamond corresponds to a 3-D calculation presented here with $f = 0.3$ and is reasonably well fit by the equation given by Yao et al. (2014) despite the fact that those authors did not include data for stagnant-lid cases with $f < 0.5$ in their parameterization.

In Figure 11b we plot contours of constant middepth Rayleigh number, Ra_{m} in $F_{\text{bot}} - f$ space. Perfect agreement between the parameterization for F_{bot} and observations would result in the diamonds falling on top

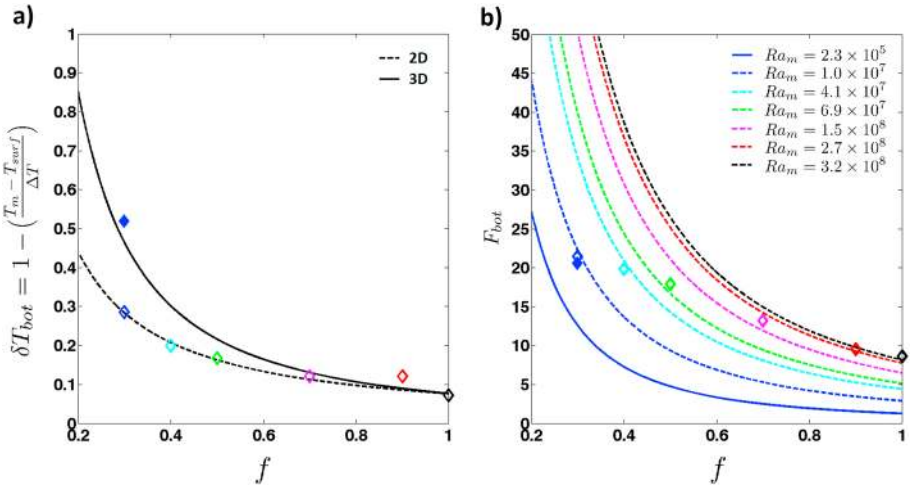

Figure 11. (a) Temperature drop across the bottom thermal boundary layer as determined from equation (10) plotted as a function of f. The solid black curve indicates temperature contrast with the value of β derived by Yao et al. (2014) for 3-D spherical shell results. The dashed black curve is the temperature drop, δT_{bot}, derived from 2-D spherical annulus results. (b) Basal heat flux plotted as a function of f. Each curve correspond to a constant value of the middepth Rayleigh number, as indicated in the key. The solid blue curve is determined from the basal heat flux equation derived for 3-D spherical shell results and the dashed colored curves are derived from the heat flux equation corresponding to 2-D spherical annulus results. Plotted diamonds indicate observations of F_{bot} for cases with corresponding f and a middepth Rayleigh number defined by color. Ra $= 3.2 \times 10^5$ for all plotted data points and $\Delta\eta_T = 10^7$ for both the observations and the calculation of the constant Ra curves. The colors of the open diamonds correspond to the same f values plotted in Figure 2 and the solid diamond represents the 3-D spherical shell case shown in Figure 9.

of the curves of corresponding color. The position of each contour is determined by the value of γ. Here we present the results for $\Delta\eta_T = 10^7$ in order to incorporate the 3-D result. Generally, the parameterization of the results for the annuli geometry is successful but the observed heat flux in the 3-D case tested is much higher than expected for the corresponding Ra_m. This could be explained by the fact that a robust lower thermal boundary layer exists in this 3-D calculation making it distinct from the cases used to determine the 3-D parameterization.

5.2. Relatively Small Cores

Figure 12 plots snapshots of the profile of the second invariant of the stress tensor, τ, (at the base of the stagnant lid) for $f = 0.3$ and 0.5 spherical annuli cases and a 10×1 plane layer case, where each system features a viscosity contrast of $\Delta\eta_T = 10^7$. The horizontal coordinates in the figure are determined by the nondimensional circumference $2\pi/(1-f)$ and position along the x axis is plotted in units of mantle depth. As curvature is increased (f decreased) the stress oscillates on a much longer wavelength in comparison to stress in the relatively large core and plane layer cases (in agreement with the finding that we observe fewer convection cells in cases with smaller cores). In addition, stress magnitude increases with increasing curvature and the $f = 0.3$ spherical annulus has a mean stress about an order of magnitude larger than the plane-layer case. The higher stresses observed at the base of the stagnant lid when f is smaller are a result of higher viscosity, due to cooler temperatures, and the presence of (relatively hot) active upwellings driving relatively longer convection cells. Together these phenomena resist the formation of a stagnant lid, providing an explanation for the observation that larger viscosity contrasts are needed to induce a stagnant lid as the curvature increases.

In Figure 13 we plot the nondimensional basal heat flux as a function of nondimensional time from annuli calculations. In addition to the mean nondimensional basal heat flux increase with decreasing f it can be seen that the variability in the heat flux increases with decreasing f. Because an increasingly robust basal thermal boundary layer is established with smaller f values, we suggest this finding is consistent with greater temporal variability in the thermal boundary layer thickness resulting from plume mobility and thermal detachment. However, in contrast to the variable time series shown in Figure 13, we find that the 3-D systems shown in Figure 9 become decreasingly time dependent as f is decreased, to the point where nearly steady planforms

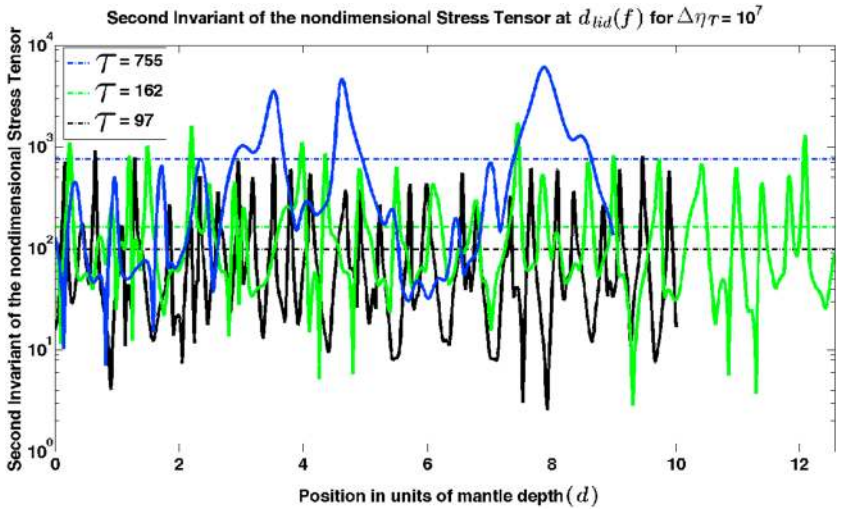

Figure 12. Example snapshots of the second invariant of the stress tensor, τ, at the base of the stagnant lid, as a function of position. Colors correspond to $f = 0.3$ (blue) and 0.5 (green) spherical annuli cases and a 10×1 plane layer case (black). All cases are characterized by a viscosity contrast of $\Delta\eta_T = 10^7$. Dot-dashed lines denote the mean of the curves with values given in the inset at the upper left.

are established when $f \leq 0.3$. A steadier flow therefore accompanies the cooler 3-D cases (e.g., see Figure 8) in accord with their lower effective Ra.

5.3. Modeling Thin Shells

In Figure 8, it was observed that 2-D models lag 3-D models in reaching the onset of SLC (for example, compare solid triangles with corresponding open square data points). In Figure 4, when $\Delta\eta_T = 10^5$ we found that both $f = 1.0$ and 0.9 cases occupy the transitional regime. However, the onset of SLC was observed for a small

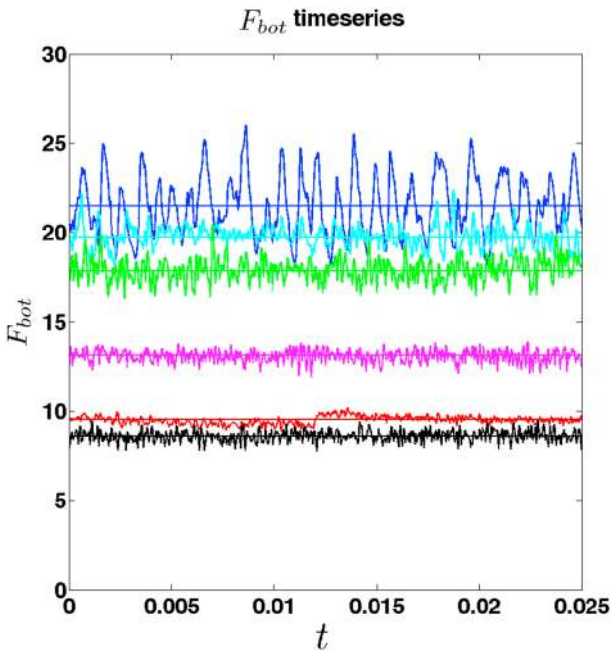

Figure 13. Time series for basal heat flux for 2-D annuli cases with variable core sizes. The time series shown correspond to the cases that yield the data points included in Figure 11 (where $\Delta\eta_T = 10^7$). Color corresponds to associated f value as previously. The solid horizontal lines indicate the mean value of the heat flux over the time interval plotted where the means (with associated standard deviations) and mobilities, M, are (blue) $\bar{F}_{\text{bot}} = 21.5 \pm 1.5$, $M = 0.0046 \pm 0.0006$; (cyan) $\bar{F}_{\text{bot}} = 19.7 \pm 0.6$, $M = 0.0009 \pm 0.0001$; (green) $\bar{F}_{\text{bot}} = 17.9 \pm 0.6$, $M = 0.0004 \pm 0.0003$; (magenta) $\bar{F}_{\text{bot}} = 13.1 \pm 0.3$, $M = 0.0010 \pm 0.0008$; (red) $\bar{F}_{\text{bot}} = 9.5 \pm 0.1$, $M = 0.0022 \pm 0.0001$; (black) $\bar{F}_{\text{bot}} = 8.6 \pm 0.3$, $M = 0.00003 \pm 0.00001$.

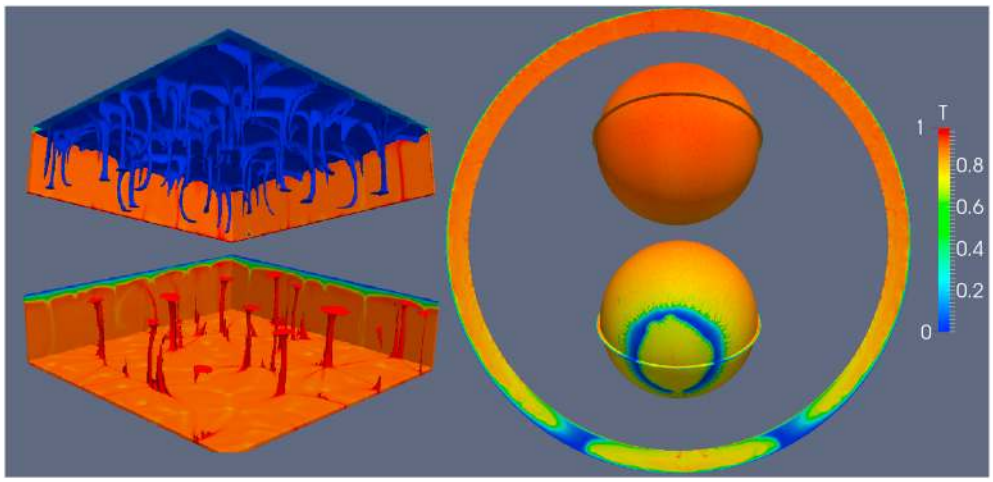

Figure 14. Temperature field snapshots in 3-D geometries. On the left the interior of a $4 \times 4 \times 1$ plane layer is shown with upwellings in red ($[T - T_{surf}]/\Delta T = 0.95$) and downwellings in blue ($[T - T_{surf}]/\Delta T = 0.85$; the isosurface colors do not correspond to the color bar). On the right the temperature in a $f = 0.9$ shell is shown at a radius of $9.5d$ ($R_{core} = 9d$, $R_{outer} = 10d$) from diametrically opposed viewing angles. A Rayleigh number $Ra = 3.2 \times 10^5$ and a viscosity contrast of $\Delta\eta_T = 10^5$ are used for both models. The resolution of the plane layer is $128 \times 512 \times 512$. The resolution of the thin-shelled sphere is $2 \times (192 \times 1152 \times 96)$. See supporting information Table S5 for input and output parameters.

increase in $\Delta\eta_T$ when $f = 1.0$. In Figure 14 we plot temperature fields from two 3-D calculations that are in agreement with the findings indicated in Figures 4 and 8. The $f = 1.0$ case is in the stagnant-lid regime, the $f = 0.9$ is not. In the $f = 1.0$ case the presence of a stagnant lid could be due to either the larger aspect ratio or simply the dimensionality effect. The plane-layer 3-D case is similar to cases presented in previous studies (e.g., Deschamps & Lin, 2014) and features cylindrical plumes and downwellings, in contrast to the sheets in our 2-D plane-layer model. In particular, it differs dramatically from the spherical thin shell ($f = 0.9$) case that features a hemispherical dichotomy characterized by a large "ring-like" downwelling in one hemisphere. The persistence of robust downwellings in the $f = 0.9$ case was observed in $f = 0.9$ annuli in Figure 1. In 3-D downwelling flow is maintained and forms a robust planform separating diametrically opposed regions of upwelling with differing volumes.

6. Conclusions

Our calculations demonstrate that core geometry strongly affects estimates of the thermal viscosity contrast required to obtain SLC. For example, in the Cartesian geometry case modeled, with the Rayleigh number specified (e.g., Figure 4), the onset of SLC occurs with a viscosity contrast more than 2 orders of magnitude less than in the $f = 0.2$ case. Core geometry also strongly affects the effective Rayleigh number for a given viscosity contrast (Figure 5) and viscosity structure in the convecting region below the stagnant-lid also changes as f is varied. For example, plots of the azimuthally averaged temperature (Figure 2) show that the isoviscous approximation for the convective layer underlying the stagnant lid is justifiable for $f \geq 0.5$ but breaks down for $f \leq 0.4$.

A comparison of SLC in two- and three-dimensional spherical geometries finds that for systems characterized by identical parameters, when $f < 0.5$, mean temperature in statistically steady systems with different dimensionalities may disagree by more than 25% and basal heat flux by more than 50%. Disagreement depends on f and the viscosity contrast modeled. With a fixed Rayleigh number, Ra, we find that for SLC in two dimensions when $f < 0.5$ the viscosity contrast established across the upper thermal boundary layer increases relative to three-dimensional convection. Similarly, the viscosity contrast across the thermal boundary layer enveloping the core is decreased by 2-D modeling (e.g., Figure 9).

In small-f systems, vigorous active upwellings persist below sluggish lids and impart surface stresses that resist the onset of SLC. Our findings may therefore help explain observations of disrupted surfaces that have been inferred to be the result of early convection in ice shells in moons with small rocky cores (Hammond & Barr, 2014). Specifically, although we have not modeled surface yielding, the higher stresses we observe

in the stagnant lids of small-core systems imply that deformation could result more readily than previously understood due to the focused plumes that characterize such systems (see Figure 12).

The results presented in this work are obtained with just one value for the reference Rayleigh number (with the exception of the cases compared to the results from Yao et al., 2014, in Figure 8). Previously, Yao et al. (2014) and Yanagisawa et al. (2016) discussed that convective regime (i.e., stagnant lid vs. mobile lid) is highly dependent on the reference Rayleigh number as well as the viscosity contrast modeled. (Studies featuring yield stresses have also noted that a higher reference Rayleigh number promotes surface mobility (e.g., Stein et al., 2004, 2014).) Consequently, our findings do not imply that a smaller body with a smaller core, like the Moon, is necessarily less likely to be characterized by a stagnant lid than the Earth, with its higher mantle Rayleigh number. Moreover, smaller cores will be depleted of their heat more quickly when secular cooling is modeled. This effect, in particular, should be the subject of further studies of the impact of core size on the convective regime of an overlying mantle of rock or ice.

In annuli, as viscosity contrast is increased to produce a stagnant lid, robust thermal boundary layers continue to envelop the relatively small cores of the systems allowing for strong time dependence of the heat flux from the core. However, in cooler interior 3-D systems, hot, core-enveloping boundary layers are less time dependent due to lower effective Ra for the systems. An increase in plume vigor with small f and the fact that planform differs substantially in 2-D and 3-D models may contribute to the divergence of 2-D and 3-D findings when f is small. Studies of isoviscous convection have previously reported breakdowns in the parameterization of mean temperature when systems featuring downwelling sheets are compared with systems featuring cylindrical downwellings (Jarvis, 1993; Shahnas et al., 2008). Our findings indicate that core heat flux time series from small-core 2-D models amplify the degree of time dependence expected in 3-D systems.

Very long wavelength flow was commonly observed in thin shelled systems so that downwellings sourcing material from a sluggish upper thermal boundary layer remain especially persistent as viscosity contrast is increased. As a result, we found that Cartesian systems can poorly emulate thin shelled cases when the aspect ratio of the former does not match the circumference of the latter. In particular, we find that the onset of transitional and SLC in a relatively smaller aspect ratio occurs at a lower viscosity contrast. For example, the circumference of an $f = 0.9$ annulus exceeds the rectangular geometry aspect ratio 10 case by more than a factor of 6 so that parameters yielding SLC in the latter geometry resulted in mobile convection in the former case. In three dimensions we observe similar behavior and thin shell solutions characterized by a hemispherical dichotomy.

Taken collectively, the findings presented here indicate that caution should be applied when extrapolating the findings from 2-D spherical calculations to 3-D systems or when extrapolating plane-layer geometry solutions to the behavior in thin spherical shells. In contrast, Earth's geometry ($f = 0.55$) places it in the range of curvature where the results of 2-D and 3-D experiments agree more closely (at least in the stagnant-lid regime). Unfortunately, in order to explore planetary evolution, our results indicate that the most computationally demanding stagnant-lid systems are specifically the cases that should be modeled in 3-D or at least full spherical annuli. Specifically, small-core cases (which require the modeling of greater viscosity contrast in order to obtain stagnant lids) and thin shell cases (which are poorly emulated by systems with smaller aspect ratios) exhibit behavior that is highly dependent on both their curvature and dimensionality.

Acknowledgments
We are especially grateful to Eh Tan for providing a 3-D benchmark result from CitcomS. We thank Amy Barr and Matt Weller for attentive and constructive reviews. J. M. G. and J. P. L. are grateful for funding from the NSERC of Canada (fund: 327084-10). Calculations were performed on the GPC cluster at the SciNet GPC Consortium and on the Saw and Orca clusters at the Sharcnet Consortium. SciNet is funded by the Canada Foundation for Innovation under the auspices of Compute Canada, the Government of Ontario, Ontario Research Fund—Research Excellence, and the University of Toronto. This work was also made possible by the facilities of the Shared Hierarchical Academic Research Computing Network (SHARCNET: www.sharcnet.ca) and Compute/Calcul Canada. All data presented are listed in the references and tables in the supporting information.

References

Barr, A. C. (2008). Mobile lid convection beneath Enceladus' south polar terrain. *Journal of Geophysical Research*, *113*, E07009. https://doi.org/10.1029/2008JE003114

Choblet, G. (2012). On the scaling of heat transfer for mixed heating convection in a spherical shell. *Physics of the Earth and Planetary Interiors*, *206*, 31–42.

Christensen, U. R. (1984). Heat transport by variable viscosity convection and implications for the Earth's thermal evolution. *Physics of the Earth and Planetary Interiors*, *35*(4), 264–282.

Christensen, U. R. (1985). Heat transport by variable viscosity convection II: Pressure influence, non-Newtonian rheology and decaying heat sources. *Physics of the Earth and Planetary Interiors*, *37*(2-3), 183–205.

Crowley, J. W., & O'Connell, R. J. (2012). An analytic model of convection in a system with layered viscosity and plates. *Geophysical Journal International*, *188*(1), 61–78.

Davaille, A., & Jaupart, C. (1993). Transient high-Rayleigh-number thermal convection with large viscosity variations. *Journal of Fluid Mechanics*, *253*, 141–166.

Deschamps, F., & Lin, J. R. (2014). Stagnant lid convection in 3D-Cartesian geometry: Scaling laws and applications to icy moons and dwarf planets. *Physics of the Earth and Planetary Interiors*, *229*, 40–54.

Deschamps, F., Tackley, P. J., & Nakagawa, T. (2010). Temperature and heat flux scalings for isoviscous thermal convection in spherical geometry. *Geophysical Journal International*, *182*(1), 137–154.

Hammond, N. P., & Barr, A. C. (2014). Formation of Ganymede's grooved terrain by convection-driven resurfacing. *Icarus*, *227*, 206–209.
Hammond, N. P., & Barr, A. C. (2014). Global resurfacing of Uranus's moon Miranda by convection. *Geology*, *42*(11), 931–934.
Hernlund, J. W., & Tackley, P. J. (2008). Modelling mantle convection in the spherical annulus. *Physics of the Earth and Planetary Interiors*, *171*(1), 48–54.
Jarvis, G. T. (1993). Effects of curvature on two-dimensional models of mantle convection: Cylindrical polar coordinates. *Journal of Geophysical Research*, *98*(B3), 4477–4485.
Jarvis, G. T., Glatzmaier, G. A., & Vangelov, V. I. (1995). Effects of curvature, aspect ratio and plan form in two-and three-dimensional spherical models of thermal convection. *Geophysical Astrophysical Fluid Dynamics*, *79*(1-4), 147–171.
Kattenhorn, S. A., & Prockter, L. M. (2014). Evidence for subduction in the ice shell of Europa. *Nature Geoscience*, *7*(10), 762–767.
King, S. D. (2009). On topography and geoid from 2-D stagnant lid convection calculations. *Geochemistry, Geophysics, Geosystems*, *10*, Q03002. https://doi.org/10.1029/2008GC002250
Matsuyama, I., Nimmo, F., Keane, J. T., Chan, N. H., Taylor, G. J., Wieczorek, M. A., & Williams, J. G. (2016). GRAIL, LLR, and LOLA constraints on the interior structure of the moon. *Geophysical Research Letters*, *43*, 8365–8375. https://doi.org/10.1002/2016GL069952
Moore, W. B. (2008). Heat transport in a convecting layer heated from within and below. *Journal of Geophysical Research*, *113*, B11407. https://doi.org/10.1029/2006JB004778
Multhaup, K., & Spohn, T. (2007). Stagnant lid convection in the mid-sized icy satellites of Saturn. *Icarus*, *186*(2), 420–435.
Nimmo, F., Giese, B., & Pappalardo, R. T. (2003). Estimates of Europa's ice shell thickness from elastically-supported topography. *Geophysical Research Letters*, *30*(5), 1233. https://doi.org/10.1029/2002GL016660
Noack, L., & Breuer, D. (2013). First-and second-order Frank-Kamenetskii approximation applied to temperature-, pressure- and stress-dependent rheology. *Geophysical Journal International*, *195*(1), 27–46.
O'Farrell, K. A., Lowman, J. P., & Bunge, H. P (2013). Comparison of spherical-shell and plane-layer mantle convection thermal structure in viscously stratified models with mixed-mode heating: Implications for the incorporation of temperature-dependent parameters. *Geophysical Journal International*, *192*, 456–472. https://doi.org/10.1093/gji/ggs053
O'Neill, C., Lenardic, A., Weller, M., Moresi, L., Quenette, S., & Zhang, S. (2016). A window for plate tectonics in terrestrial planet evolution? *Physics of the Earth and Planetary Interiors*, *255*, 80–92.
O'Neill, C., & Nimmo, F. (2010). The role of episodic overturn in generating the surface geology and heat flow on Enceladus. *Nature Geoscience*, *3*(2), 88–91.
Reese, C. C., Solomatov, V. S., Baumgardner, J. R., & Yang, W. S. (1999). Stagnant lid convection in a spherical shell. *Physics of the Earth and Planetary Interiors*, *116*(1), 1–7.
Schubert, G., Sohl, F., & Hussmann, H. (2009). Interior of Europa. In R. T. Pappalardo, W. B. McKinnon, & K. K. Khurana (Eds.), *Europa* (pp. 353). Tuscon, AZ.
Shahnas, M. H., Lowman, J. P., Jarvis, G. T., & Bunge, H. P. (2008). Convection in a spherical shell heated by an isothermal core and internal sources: Implications for the thermal state of planetary mantles. *Physics of the Earth and Planetary Interiors*, *168*(1), 6–15.
Sohl, F., Spohn, T., Breuer, D., & Nagel, K. (2002). Implications from galileo observations on the interior structure and chemistry of the Galilean satellites. *Icarus*, *157*(1), 104–119.
Solomatov, V. S. (1995). Scaling of temperature-and stress-dependent viscosity convection. *Physics of Fluids*, *7*(2), 266–274.
Solomatov, V. S., & Moresi, L. N. (1996). Stagnant lid convection on Venus. *Journal of Geophysical Research*, *101*(E2), 4737–4753.
Sotin, C., & Labrosse, S. (1999). Three-dimensional thermal convection in an iso-viscous, infinite Prandtl number fluid heated from within and from below: Applications to the transfer of heat through planetary mantles. *Physics of the Earth and Planetary Interiors*, *112*(3), 171–190.
Stein, C., Lowman, J. P., & Hansen, U. (2013). The influence of mantle internal heating on lithospheric mobility: Implications for super-Earths. *Earth and Planetary Science Letters*, *361*, 448–459.
Stein, C., Lowman, J. P., & Hansen, U. (2014). A comparison of mantle convection models featuring plates. *Geochemistry, Geophysics, Geosystems*, *15*, 2689–2698. https://doi.org/10.1002/2013GC005211
Stein, C., Schmalzl, J., & Hansen, U. (2004). The effect of rheological parameters on plate behaviour in a self-consistent model of mantle convection. *Physics of the Earth and Planetary Interiors*, *142*(3-4), 225–255.
Tackley, P. J. (2000). Self-consistent generation of tectonic plates in time-dependent, three-dimensional mantle convection simulations. *Geochemistry, Geophysics, Geosystems*, *1*(8), 1021. https://doi.org/10.1029/2000GC000036
Tackley, P. J. (2008). Modelling compressible mantle convection with large viscosity contrasts in a three-dimensional spherical shell using the yin-yang grid. *Physics of the Earth and Planetary Interiors*, *171*(1), 7–18.
Vangelov, V. I., & Jarvis, G. T. (1994). Geometrical effects of curvature in axisymmetric spherical models of mantle convection. *Journal of Geophysical Research*, *99*(B5), 9345–9358.
Weber, R. C., Lin, P. Y., Garnero, E. J., Williams, Q., & Lognonne, P. (2011). Seismic detection of the lunar core. *Science*, *331*(6015), 309–312.
Weller, M. B., & Lenardic, A. (2012). Hysteresis in mantle convection: Plate tectonics systems. *Geophysical Research Letters*, *39*, L10202. https://doi.org/10.1029/2012GL051232
Weller, M. B., Lenardic, A., & Moore, W. B. (2016). Scaling relationships and physics for mixed heating convection in planetary interiors: Isoviscous spherical shell. *Journal of Geophysical Research: Solid Earth*, *121*, 7598–7617. https://doi.org/10.1002/2016JB013247
Weller, M. B., Lenardic, A., & O'Neill, C. (2015). The effects of internal heating and large scale climate variations on tectonic bi-stability in terrestrial planets. *Earth and Planetary Science Letters*, *420*, 85–94.
Yanagisawa, T., Kameyama, M., & Ogawa, M. (2016). Numerical studies on convective stability and flow pattern in three-dimensional spherical mantle of terrestrial planets. *Geophysical Journal International*, *206*(3), 1526–1538.
Yao, C., Deschamps, F., Lowman, J. P., Sanchez-Valle, C., & Tackley, P. J. (2014). Stagnant lid convection in bottom-heated thin 3-D spherical shells: Influence of curvature and implications for dwarf planets and icy moons. *Journal of Geophysical Research: Planets*, *119*, 1895–1913. https://doi.org/10.1002/2014JE004653